

The effects of strong temperature anisotropy on the kinetic structure of collisionless slow shocks and reconnection exhausts. Part I: PIC simulations

Yi-Hsin Liu, J. F. Drake, and M. Swisdak
University of Maryland, College Park, MD 20742
 (Dated: March 21, 2022)

A 2-D Riemann problem is designed to study the development and dynamics of the slow shocks that are thought to form at the boundaries of reconnection exhausts. Simulations are carried out for varying ratios of normal magnetic field to the transverse upstream magnetic field (*i.e.*, propagation angle with respect to the upstream magnetic field). When the angle is sufficiently oblique, the simulations reveal a large firehose-sense ($P_{\parallel} > P_{\perp}$) temperature anisotropy in the downstream region, accompanied by a transition from a coplanar slow shock to a non-coplanar rotational mode. In the downstream region the firehose stability parameter $\varepsilon = 1 - \mu_0(P_{\parallel} - P_{\perp})/B^2$ tends to lock in to 0.25. This balance arises from the competition between counterstreaming ions, which drives ε down, and the scattering due to ion inertial scale waves, which are driven unstable by the downstream rotational wave. At very oblique propagating angles, 2-D turbulence also develops in the downstream region.

I. INTRODUCTION

Following the publication of the MHD reconnection scenario of Sweet and Parker [1, 2], Petschek [3] noted that a pair of back-to-back slow shocks bounding the reconnection outflow could significantly raise the efficiency of the process by acting as a transition between the inflowing and reconnected outflowing plasma. Ion heating by these Petschek-reconnection-associated slow shocks is one of the mechanisms that has been proposed for solar flares [4, 5] and the solar wind. However, although in-situ observations of slow shocks in the solar wind exist [6–11], they are relatively rare, suggesting that the MHD picture of Petschek may not tell the complete story. Unanswered questions remain concerning the kinetic structure of such shocks in a collisionless plasma and the associated mechanisms leading to particle heating. In previous work, kinetic slow shocks were studied numerically in hybrid codes by initializing the system with the slow shock jumps predicted by MHD [12] or, later, by the piston [13] and flow-flow methods [14]. Some of the main focuses of these works were the backstreaming beam-driven electromagnetic ion-ion cyclotron instability (EMIIC) [13, 14], which has been suggested to be the cause of the nonsteady behavior of slow shocks, and the formation and damping of downstream large amplitude dispersive wavetrains [12, 15]. Recently, the dissipation due to electrons and beam-excited kinetic Alfvén waves was studied by the piston method in particle-in-cell (PIC) simulations [16, 17].

In PIC simulations of reconnection, the plasma downstream of the X-line exhibits large firehose-sense ($P_{\parallel} > P_{\perp}$) temperature anisotropies, as shown in Fig. 1. (This simulation was discussed previously [18]). Panel (a) shows the out-of-plane electron current, with the X-point at $(x/d_i, z/d_i) \sim (0, 20)$, where d_i is the ion inertial scale. In panels (b) and (c), we see turbulence in the B_x component correlated with the unstable firehose region; a cut of the firehose stability parameter $\varepsilon = 1 - \mu_0(P_{\parallel} - P_{\perp})/B^2$ at $z = -35d_i$ is shown in (d). The firehose-sense temperature anisotropy is notable since in-situ observations of the solar wind clearly show that the proton temperature anisotropy is bounded by the marginal firehose and mirror mode stability boundaries [19]. Hence, it is of interest to more closely study the temperature anisotropy distribution across the reconnection exhaust far downstream from the reconnection site, in order to understand the effect of the self-generated temperature anisotropy on the propagation and steepening of the slow shock.

The Petschek theory of reconnection [3] predicts that the reconnection exhaust will be bounded by a back-to-back pair of standing switch-off slow shocks. However, no clear signature of Petschek shocks has been seen in PIC reconnection simulations, such as in Fig. 1 [18], or hybrid simulations [20, 21]. This may be due to the relatively small domain sizes in the shock normal direction (\hat{e}_x in Fig. 1), although other reasons have been discussed in the context of large-scale hybrid reconnection simulations [20, 22]. To address this issue, we perform 2-D PIC simulations that extend the simulation size in the normal direction to $\sim 800d_i$ by ignoring the X-line and instead examining the conceptually simpler Riemann problem. In the Riemann formulation, waves propagate away from an interface of two different uniform states, such as the two sides of a reconnection symmetry line. This set-up more closely resembles the reconnection outflow exhaust than that produced by other methods of generating shocks. Similar Riemann problems have been carried out in 1-D resistive-MHD [15], including analyses of asymmetric states and the effect of a guide field, and in 1-D hybrid simulations [22]. 2-D Riemann problems have also been carried out in hybrid simulations [23] where the 2-D downstream turbulence appeared to diminish the downstream wavetrains associated with switch-off slow shocks. Upstream perpendicular heating by EMIIC and the subsequent excitation of Alfvén/ion cyclotron waves

have also been studied in similar 2-D Riemann problems [24, 25].

In Sec. II of this paper we introduce our simulation model and the initial set-up of the Riemann problem. In Sec. III we discuss the general profiles of a run with $\theta_{BN} = 75^\circ$ (the angle between the upstream magnetic field and the normal direction (\mathbf{e}_x)). Section IV points out that the counterstreaming ions drive ε down (increase the firehose-sense temperature anisotropy) in the downstream region. In Sec. V we show that a more oblique angle results in a lower ε at downstream region. The structure of the magnetic field performs a transition from a coplanar decrease to a non-coplanar rotation at $\varepsilon \sim 0.25$, which differs from the traditional slow shock transition with dispersive wavetrains. In Sec. VI the stability of the downstream rotational wave is studied with numerical experiments. The tendency for a spatially modulated rotational wave to radiate d_i -scale waves is identified. The resulting d_i -scale waves counter-balance the ε decrease driven by the counterstreaming ions. Finally, we summarize the results and discuss potential implications in Sec. VII.

II. SIMULATION MODELS AND DETAILS

Our PIC simulations use a narrow computational domain, $l_z \times l_x = 1.6d_i \times 1638.4d_i$ to capture the nonlinear wave propagation (mainly the slow shock pair in Petschek's reconnection model) far downstream from the reconnection site. The strategy is to use time as a proxy for space in order to reduce the computational burden. The simulations presented here are two-dimensional, *i.e.*, $\partial/\partial y = 0$, and periodic in the $z - x$ plane. The initial equilibrium consists of a double Harris-like current sheet (although we only focus on a single current sheet) superimposed on an ambient population of uniform density n_a :

$$B_z = B_{z,a} \tanh(x/w_i); \quad n_{p,e} = n_h \text{sech}^2(x/w_i) + n_a, \quad (1)$$

where $B_{z,a}, n_h, n_a$ are constants, the subscript ‘‘a’’ stands for the asymptotic (far upstream) values, ‘‘h’’ stands for Harris and w_i is the initial half-width of the current sheet. We initialize both the Harris plasma and background plasma with an isotropic Maxwellian distribution. Unlike the initial set-up for reconnection, we begin with a constant normal field B_x . Although the initial total pressure is balanced, the existence of B_x causes a tension force that drives wave propagation away from the current sheet in the x -direction. The $B_{x,a}/B_{z,a} = 0.1$ case (*i.e.*, $\theta_{BN} \sim 83^\circ$ with $\cos \theta_{BN} \equiv B_{x,a}/B_a$) corresponds to a reconnection exhaust with a normalized reconnection rate of 0.1.

This simulation box can be pictured as existing in the reconnection outflow frame. The distance from the reconnection site is estimated as $C_{Az} \times \text{time}$, where $C_{Az} \equiv B_{z,a}/\sqrt{\mu_0 m_i n_a}$ is the Alfvén speed based on the reversed component of the field. When l_z is small our simulations are essentially 1-D, although we do perform runs with larger l_z to investigate the possibility of developing 2-D turbulence. Waves (*e.g.*, fast, intermediate, and slow modes in the fluid model) will propagate away from the central discontinuity at their characteristic speeds, and can steepen into shocks, spread into rarefactions, or maintain their initial shapes based on their own nonlinearities.

In our particle-in-cell code p3d [26], the electromagnetic fields are defined on gridpoints and advanced in time with an explicit trapezoidal-leapfrog method using second-order spatial derivatives. The Lorentz equation of motion for each particle is evolved by a Boris algorithm where the velocity \mathbf{v} is accelerated by \mathbf{E} for half a timestep, rotated by \mathbf{B} , and accelerated by \mathbf{E} for the final half timestep. To ensure that $\nabla \cdot \mathbf{E} = \rho/\epsilon_0$ a correction electric field is calculated by inverting Poisson's equation with a multigrid algorithm.

The magnetic field is normalized to the asymptotic magnetic field B_a , the density to the asymptotic density n_a , velocities to the Alfvén speed $C_A \equiv B_a/\sqrt{\mu_0 m_i n_a}$, lengths to the ion inertial length $d_i \equiv \sqrt{m_i/\mu_0 n_a e^2}$, times to the inverse ion cyclotron frequency $\Omega_{ci}^{-1} \equiv m_i/B_a e$, and temperatures to $m_i C_A^2$. Other important parameters are $m_i/m_e = 25$, $c/C_A = 15$, $n_a = 1$, $n_h = 1.5$, $B_a = 1$, and the asymptotic value of initial $T_{i,e} = 0.1$, which implies that $\beta_a = 0.4$. The initial electron temperature is uniform, while the ion temperature varies so as to ensure pressure balance in the x -direction. We take the time step $\Delta t = 0.0025$ and grid size $\Delta = 0.025$. We usually take $w_i = d_i$ since the thickness of the dissipation region during reconnection is on the d_i scale. There are $\sim 4 \times 10^8$ particles in a single run. Table I gives further details of the various runs.

Runs **a**, **b**, **c**, **d**, **f**, **g**, **h** and **k** (all have $l_z = 1.6d_i$, except the $\theta_{BN} = 83^\circ$ case) will be further discussed in this work. Even though the 75° case with a larger $l_z = 6.4d_i$ (Run **i**) shows downstream 2-D turbulence, the evolution is quite similar to the narrow Run **f**. As can be seen in TABLE I, 2-D turbulence tends to occur for oblique ($\theta_{BN} > 75^\circ$) cases when l_z is large enough. Curves plotted throughout the rest of this paper are quantities averaged in the z -direction, since most runs discussed here do not have any significant variation in the z -direction. The 2-D turbulence of $\theta_{BN} = 83^\circ$ (Run **k**) will also be discussed.

III. GENERAL FEATURES OF THE 75° CASE

A representative case of $\theta_{BN} = 75^\circ$, $w_i = 1d_i$, $B_g = 0$ (Run **f**; hereafter referred to as the “75° run”) at time $200/\Omega_{ci}$ is documented in Fig. 2. As soon as the simulation begins, a pair of fast rarefaction waves propagate out from the discontinuity with speed $\sim 1.1C_A$, while the slow shocks with their downstream rotational waves have speed $\sim 0.15C_A$. As in ideal MHD with a symmetric initial condition and zero guide field, a pair of switch-off slow shocks are expected to follow the fast rarefaction waves, as shown in Fig. 2(b) [15]. A switch-off slow shock (*i.e.*, the strongest slow shock, whose tangential magnetic field vanishes downstream of the shock) propagates at the upstream intermediate speed, while the downstream linear slow mode speed equals the downstream linear intermediate speed. The linear slow mode and intermediate mode are known to become degenerate at parallel propagation when the plasma β (plasma thermal pressure/magnetic pressure) exceeds 1. The downstream rotational waves are often identified as dispersive wavetrains. The essential physics of this wavetrain can be described by a two-fluid model [27], or by Hall-MHD.

Further details of the slow shock pair are shown in Fig. 3. The most significant feature differing from the ideal MHD model is the presence of a large downstream temperature anisotropy $\varepsilon \equiv 1 - \mu_0(P_{\parallel} - P_{\perp})/B^2$ shown in panel (a). The corresponding magnetic field structure is shown in panel (b), where the left-hand-polarized rotational wave is clearly seen (the polarization will be discussed further in the hodograms of Fig. 5). The value of ε drops from 1.0 upstream of the slow shock to ~ 0.25 around the nearly constant-magnitude rotational waves found downstream. The anisotropy factor ε affects the strength of the tension force, which in the fluid theory is proportional to $\varepsilon(\mathbf{B} \cdot \nabla)\mathbf{B}/\mu_0$. When ε is positive, the magnetic field has a restoring tension force, while a negative value makes the tension force operate in the opposite way, driving the firehose instability. Viewed another way, the phase speed of an intermediate mode is $C_I \equiv \sqrt{\varepsilon}C_A \cos(\theta_{BN})$. Therefore, as ε drops the intermediate mode becomes slower, or even stops propagating, going firehose unstable for $\varepsilon < 0$. The x -direction heat flux $Q_x \equiv \int d^3v (\frac{1}{2}m\delta v^2 \delta v_x) f$, where $\delta \mathbf{v} \equiv \mathbf{v} - \langle \mathbf{v} \rangle$, is also documented in (a). The heat flux peaks inside the transition from upstream of the slow shock to the downstream rotational waves, and then becomes negligible. This fact is used in the follow-up paper [28]. In panel (c), the parallel ion temperature increases sharply in the weak field region, while the perpendicular ion temperature is nearly constant. The electrons are nearly isotropic across the shock. In panel (d), the parallel plasma pressure and perpendicular plasma pressure are shown, and the nearly constant normal direction pressure balance $P_x + B^2/2\mu_0$ indicates the absence of fast modes in the reversal region. Panel (e) shows the associated variations in β and the local θ_{BN} and panel (f) documents the density profiles. In order to pin down important kinetic effects not included in the MHD model (such as the large temperature anisotropy), the black dotted curves in each panel show the predicted jumps and positions of slow shocks in the ideal MHD version of this global Riemann problem [15].

Within the MHD predicted switch-off slow shock (SSS) jump shown in panel (b), a coplanar transition decreases the SSS upstream B_z to ~ 0.5 . After this, the magnetic field structure rotates in the non-coplanar direction and exhibits nearly constant $|B|$ inside the downstream rotational waves. The amplitude eventually drops to the value of B_x (*i.e.*, the tangential magnetic field vanishes) in the center, as the symmetry of the initial conditions demands. The coplanar transition is recognizable as a slow shock transition, where the major enhancements of the temperatures, pressures, densities and decrease in $|B|$ occur. A similar step-like decrease in $|B|$ due to a slow shock was also noted in the downstream of a large-scale hybrid reconnection simulation [20]. The constancy of the total magnetic field inside the downstream rotational wave suggests an intermediate-wave-like behavior.

IV. THE SOURCE OF TEMPERATURE ANISOTROPY: ALFVÉNIC COUNTER-STREAMING IONS

Using the Walen relation $\mathbf{V}_{t,d} - \mathbf{V}_{t,u} = \pm \sqrt{\rho_u \varepsilon_u / \mu_0} (\mathbf{B}_{t,d} / \rho_d - \mathbf{B}_{t,u} / \rho_u)$ for switch-off slow shocks or rotational discontinuities (“t” for tangential, “u” for upstream and “d” for downstream), an outflow in the z -direction with Alfvénic velocity, $B_{z,u} / \sqrt{\mu_0 \rho_u} \sim C_{Az} \equiv B_{z,a} / \sqrt{\mu_0 m_i n_a}$ is predicted [29]. The energy source of the downstream outflow is the difference in the tangential component of the magnetic field across the discontinuity. If we jump to the outflow frame (the de Hoffmann-Teller frame), there will be inflowing Alfvénic streaming ion beams from both discontinuities along the downstream magnetic field as observed by Gosling in the solar wind [30] and in kinetic reconnection simulations [18, 20, 21, 31, 32]. These counter-streaming ions cause an enhancement in the downstream parallel ion temperature and, therefore, the temperature anisotropy.

In the phase space of the 75° case at time $200/\Omega_{ci}$ (see Fig. 4) a signature of the counter-streaming beams is not obvious in the downstream region (since the ion distribution does not peak in the upper and lower parts of a single wave oscillation), perhaps because of the large-amplitude rotational wave. However, Alfvénic backstreaming ions in the z -direction (close to the parallel direction in the upstream region) are observed in Fig. 4. The time-of-flight effect (faster ions escape farther upstream) slowly broadens the transition region of slow shocks with time. The nearly uniform electron distribution in all directions is due to their high thermal conductivity and much lighter mass

compared to the ions.

V. TEMPERATURE ANISOTROPY VS. PROPAGATION ANGLES

In order to understand how the temperature anisotropy varies with other parameters, we perform runs with different upstream angles θ_{BN} . Fig. 5 documents the results of Runs **a**, **b**, **c**, **d**, **f** and **k**. From the first column, the downstream ε tends to lower values in the more oblique cases and the plasma becomes turbulent once ε is comparable to or lower than ~ 0.25 . We can estimate at which θ_{BN} the downstream ε will drop below 0.25 as follows. In the cold plasma limit, the temperature anisotropy due to the Alfvénic counter-streaming ions at the symmetry line is (where $P_{\parallel} - P_{\perp} \sim n_a m_i C_{Az}^2$ and $|B| \sim B_{x,a}$),

$$\varepsilon_{down} \sim 0.25 \sim 1 - \frac{B_{z,a}^2}{B_{x,a}^2} \quad \rightarrow \tan^2 \theta_{BN,c} \sim 0.75 \quad \rightarrow \theta_{BN,c} \sim 40^\circ \quad (2)$$

This argument qualitatively shows the tendency to develop stronger firehose-sense temperature anisotropies for higher obliquities. The difference between $\theta_{BN,c}$ and the observed value of 60° is probably due to the simplified assumptions, such as a cold streaming plasma.

In the second column of Fig. 5, the corresponding magnetic structures are shown. When the obliquity is large enough, especially when $\varepsilon < 0.25$, the downstream magnetic field rotates into the out-of-plane direction and becomes turbulent. Combined with the hodograms in the third column, we can deduce that the dominant downstream rotational waves are all left-handed (LH, counter-clockwise in our hodogram). When the wavelength of the primary LH wave is large, as in the $\theta_{BN} = 60^\circ$ case, its front part breaks into finer right-handed (RH) waves with scale $\sim 6d_i$. In the 75° case, the scale of the primary LH wave is already as small as $6d_i$, and so it is more stable than the 60° case, albeit still turbulent. (A 75° case with a wider initial current layer is discussed in the next section. It exhibits wave-generation phenomena similar to the 60° case). In the 83° case, we observe RH small-scale waves in front of the downstream primary LH wave.

For comparison, the dotted curves in the second column of Fig. 5 are the predicted B_z structure from MHD theory [15]. The overall predictions agree well for the oblique cases (see, for instance, the upstream B_z of the slow shocks in the 60° and 75° cases), although the reflected weak fast rarefactions from our boundary have caused a discrepancy in the slow shock upstream B_z for the 83° case. In less oblique cases, the intermediate and fast characteristic speeds approach one another just upstream of the switch-off slow shock according to MHD theory. Therefore there is no clear separation between the slow shocks upstream and the fast rarefactions, as can be seen in the simulations. We treat the place where the inflow speed V_x (not shown) starts to decrease as the upstream of the slow shocks, which corresponds to the beginning of the LH rotational wavetrains in the 30° and 45° cases. Their upstream will hence correspond to $B_z \sim 0.15$ and $B_z \sim 0.2$ respectively. Therefore the stable small amplitude rotational waves in the $\theta_{BN} = 30^\circ$ and 45° cases are more similar to the conventional dispersive stationary downstream wavetrains, which immediately follow the slow shock upstream. (We note that the model in Lin and Lee [15] approximates the rarefactions by replacing the energy jump condition in the Rankine-Hugoniot relations by $[P\rho^{-\gamma}] = 0$, arguing that the entropy across a weak rarefaction does not change. This is only valid for weak rarefaction waves, but the overall tendency as the propagation angle becomes more parallel should be in the correct sense).

An interesting feature in the oblique cases is the coincidence between the start of the primary LH magnetic rotation and the location where the anisotropy parameter $\varepsilon \sim 0.25$. The anisotropy parameter seems to be locked to this critical value for long periods of time, as is shown in Fig. 6. Moreover, this is also the location where turbulence develops. Given these coincidences the following questions naturally arise. If the rotational wave is really a normal dispersive wavetrain, why does it appear in the middle of the MHD predicted switch-off slow shocks? Why do the dispersive waves not start directly from the slow shock upstream? Is it not more similar to a new transition at $B_z \sim 0.3$ for $\theta_{BN} = 60^\circ$, or $B_z \sim 0.5$ for $\theta_{BN} = 75^\circ$ and 83° ? What is special about $\varepsilon = 0.25$? The importance of $\varepsilon \sim 0.25$ is shown for different obliquities in Fig. 7. Are there other instabilities associated with this anisotropy value? Or is it due to the nonlinear structure of a system with a large temperature anisotropy that cannot be explained by ideal MHD?

We describe a possible theoretical explanation for why $\varepsilon \sim 0.25$ in a follow-up paper [28]. In short, $\varepsilon = 0.25$ represents a transition where the slow and intermediate mode speeds become degenerate. Unlike the conventional picture, the downstream rotational waves can not then be explained by slow dispersive waves, but instead take the form of rotational intermediate modes. The coplanar decreasing part of the magnetic field together with the non-coplanar rotational part will later be identified as a single nonlinear wave, called a compound SS/RD wave [28].

VI. THE DOWNSTREAM TURBULENT WAVES AND PARTICLE SCATTERING

The region downstream of oblique ($\theta_{BN} \geq 60^\circ$) slow shocks is turbulent. High wavenumber waves are continually excited whenever the B_z component begins to rotate into the out-of-plane direction, as can be seen for the 60° , 75° and 83° cases in Fig. 5, and more clearly in the evolution of the B field for the case 75° , $w_i = 10d_i$ (Run **g**) in Fig. 8. The downstream LH rotational parent waves break into $\lambda_x \sim 6d_i$ -scale waves. The large oscillation in ε at later times is due to the small magnetic field magnitude near the symmetry line, where both B_z and B_y vanish. The particle scattering associated with these small-scale waves plays a role in counter-balancing the decrease in ε due to the streaming ions and keeping the temperature anisotropy around the value 0.25, as is seen in the time evolution of the oblique cases in Fig. 6.

In order to understand the downstream turbulent d_i -scale waves, we tried to systematically pin down the possible driver and energy source via numerical experiments. We separately checked potential energy sources in the shock simulations, including temperature anisotropy, counterstreaming beams, rotational parent waves (such as the larger LH wave in Fig. 8) to determine which factors are responsible for generating the d_i -scale waves.

We carried out spatially homogeneous simulations with an initial wave structure of the following form:

$$B_z = B_{\text{cir}} \cos(2\pi x/\lambda_p) + B_{z,\text{oblique}}; \quad B_y = P \times B_{\text{cir}} \sin(2\pi x/\lambda_p) \quad (3)$$

When $B_{\text{cir}} \neq 0$, there is a rotational field with $P = +1$ for LH, -1 for RH, and 0 for planar polarizations. The constant $B_{z,\text{oblique}}$ controls the obliquity of this circularly polarized wave and provides a spatial modulation in the magnitude of the total magnetic field. The general expression for the initial ion distribution is

$$f_i \propto \exp\left(-\frac{m_i(v_{\parallel} - u)^2}{2T_{i\parallel}} - \frac{m_i v_{\perp}^2}{T_{i\perp}}\right) + \exp\left(-\frac{m_i(v_{\parallel} + u)^2}{2T_{i\parallel}} - \frac{m_i v_{\perp}^2}{T_{i\perp}}\right) \quad (4)$$

which has bi-Maxwellian counterstreaming beams for $u \neq 0$. Note that $T_{i\parallel,\text{eff}} = T_{i\parallel} + m_i u^2$, so both $u \neq 0$ and $T_{i\parallel} \neq T_{i\perp}$ can contribute to the temperature anisotropy ε . The initial plasma density varies so as to ensure a constant value of $P_{\perp} + B^2/(2\mu_0)$. Since the small-scale waves that interest us do not induce variation in the z -direction, they are intrinsically 1-D waves along the x -direction. The common parameters used here are a domain size of 1.6×51.2 , with grid 64×2048 , $\lambda_p = 51.2d_i$, uniform $T_{i,e\perp} = T_{e\parallel} = 0.15$, $B_x = 0.25$ and $n_{i,e} = 1.5$ at $x = 0$. These parameters are meant to represent those observed in the downstream of the 75° case.

Run **1** of Table II is a representative example of the downstream structure seen in the Riemann simulations. The initial obliquely propagating LH polarized waves with Alfvénic counter-streaming ions along the local magnetic field break into $\sim 6d_i$ small-scale waves, as shown in Fig. 9(a). In Run **2**, we replace the counter-streaming ions with a bi-Maxwellian plasma with the same effective parallel temperature, therefore the same temperature anisotropy ε , and find similar wave-generation phenomena. In Runs **3** and **4**, we remove the obliquity ($B_{z,\text{oblique}}$) from Runs **1** and **2** respectively. No d_i -scale waves are excited within a time of $100/\Omega_{ci}$ in Run **3**, as is shown in Fig. 9(b). This indicates the importance of spatial modulation for the development of the turbulence. In Run **5**, we replace the beams or anisotropic plasma of Runs **1** and **2**, respectively, with a Maxwellian isotropic plasma. Waves with scale $\sim 6d_i$ are excited and are shown in Fig. 9(c). However, if we further remove the initial out-of-plane magnetic field of the parent wave (Run **6**), no small-scale waves appear; see Fig. 9(d). This indicates that a necessary condition for producing these small-scale waves is the existence of circularly polarized parent waves. From this suite of runs we conclude that the presence of a spatially modulated rotational wave is the major driver of d_i -scale coherent waves seen downstream of the shock (see Fig. 8(b)). Although not shown, we see similar behavior for RH ($P = -1$) parent waves.

A non-modulated, constant-amplitude, circularly polarized Alfvén wave is a known stationary solution of the MHD equations. Although it is subject to a long-wavelength modulational instability under some conditions [33], simulations show that it is also stable in a collisionless plasma. Spangler [34] explored a similar wave-generation phenomena, as well as the formation of solitary waves with a system with initial conditions similar to our Run **5**. He cast his system in terms of the Derivative-Nonlinear-Schrödinger-Equations, which are simplified MHD equations that possess the MHD nonlinearity and dispersion terms. This suggests the importance of both the nonlinearity and the Hall dispersion term for these d_i -scale waves. We also note that the time of onset of these waves is proportional to λ_p and inversely proportional to the amplitude B_{cir} , which are closely related to the steepening time scale of finite amplitude waves, $T_s \sim (\tau_{\text{wave}}/2\pi)(B/\Delta B)$, with $\tau_{\text{wave}} \propto \lambda_p$ (the gradient scale of the finite amplitude wave) [35]. Although a firehose-sense temperature anisotropy ($\varepsilon < 0$) would weaken the nonlinearity, the spatial variation of ε enhances the nonlinearity, as will be shown in the follow-up paper [28].

Runs **3** and **4** suggest that temperature anisotropy and Alfvénic beams are not, by themselves, sufficient for generating the small-scale waves seen in the downstream region. The time scale of the wave-generation is faster than

beam/anisotropy driven waves from the electromagnetic ion-ion cyclotron instability (EMIIC), such as Alfvén/ion cyclotron (AIC) waves [36], or kinetic-Alfvén waves (KAW)[37]. As is the case for the growth rate of the firehose instability $\gamma^2 \sim (-\varepsilon k^2 C_A^2)/(1 + C_A^2/c^2)$ [38], the growth rate is small when C_A (based on the ambient B field) is small. However, these beam/anisotropy-driven waves are still potential players in the downstream turbulence at late time. By comparing Fig. 9(a) to (c), we see that the interplay of the steepening process and the free-streaming beams makes the wave more turbulent. In Fig. 10, the ion temperature anisotropy $T_{i\parallel} - T_{i\perp}$ of Run 1 (which corresponds to Fig. 9(a)) decreases. This confirms the ability of these smaller-scale dispersive waves to scatter ions.

The polarization of a linear wave can be determined by the phase between the tangential magnetic field variations δB_z and δB_y . In the fluid model $i\delta B_z/\delta B_y = (C_I^2 - (\omega/k)^2)/(\omega d_i C_A \cos(\theta_{BN}))$ [11]. A wave has a LH polarization when $(\omega/k)^2 > C_I^2$, and RH otherwise. As observed in our oblique shock simulations (discussed in Sec. V), the small-scale waves at the upstream of the rotational front are mostly RH, while the downstream waves are mostly LH. This suggests that the primary rotational front propagates at the local intermediate speed (as also measured in the simulations). We do not address which modes are responsible for these fine-scale waves here, since the polarization of the linear mode in kinetic theory is very complicated. Both temperature anisotropy and high plasma β play roles in changing the linear wave properties [39]. With a larger l_z and very oblique propagation angle, as in the 83° case, 2-D turbulence with $\lambda_z \sim 6d_i$ is excited around the firehose-unstable region. Its signature is most clear in B_x , as can be seen in the bottom plot of Fig. 6. A similar mechanism is postulated to excite 2-D turbulence in the firehose-unstable region seen in the reconnection simulation of Fig. 1(c) (and, perhaps, the 2-D turbulence previously reported [23]). This 2-D turbulence could be driven by temperature anisotropy (firehose-like) or by the sharp front of the primary rotational wave.

VII. SUMMARY AND DISCUSSION

We have studied the temperature anisotropy distribution across slow shocks with different obliquities in PIC simulations. An abnormal transition and an anisotropy $\varepsilon = 0.25$ locking phenomena downstream of the MHD predicted switch-off slow shocks is documented. The Alfvénic counter-streaming ions serve as the driver for decreasing ε (increasing the firehose-sense temperature anisotropy) in the downstream region, while downstream d_i -scale turbulent waves scatter particles and raise ε . This dynamical balance makes the downstream ε plateau at a value of $\varepsilon = 0.25$ and not the marginal firehose criterion $\varepsilon = 0$. The theoretical significance of $\varepsilon = 0.25$ will be addressed in another work [28]. By means of PIC numerical experiments we show that the turbulent d_i -scale waves are radiated from a spatially modulated rotational parent wave.

The Riemann problem for the $\theta_{BN} = 83^\circ$ case is closely related to that of reconnection exhausts with normalized reconnection rates of 0.1. The very center is a firehose-unstable region where a B_x variation is observed, as in the reconnection simulations. Although we cannot confidently identify the 0.25 plateau in present PIC reconnection simulations (since the spatial extension in the normal direction (\hat{e}_x), is $\sim 10d_i$; see Fig. 1(d)), we expect to see the signature of a $\varepsilon = 0.25$ plateau outside the firehose unstable region in very large kinetic anti-parallel reconnection simulations and in-situ satellite observations of anti-parallel magnetic reconnection outflows.

Compared to slow shocks, fast shocks have been intensively studied (see, for instance, a review article [40]). The formation of shocklet and short large-amplitude magnetic structures (SLAMs) in front of earth's quasi-parallel bow shock has been observed [41] and simulated [42, 43]. In our slow shock simulations, the development of downstream rotational waves produces SLAMs-like structures as in Fig. 8(b). Since the transition of the magnetic field across the front in a fast shock is opposite to that in a slow shock, if there are SLAMs associated with a slow shock, they are expected to exist in the downstream region, especially since the downstream of a switch-off slow shock is locally quasi-parallel.

Finally, even though we have not seen super-thermal particles other than Alfvénic streaming ions in our shock simulations, it is still an open question whether particles could be accelerated by slow shock associated reconnection exhausts via mechanisms recognized in fast shocks such as the 1st-order Fermi mechanism [44], diffusive shock acceleration (DSA) [45, 46], and those possible injection mechanisms for DSA such as shock-drift [47], or shock surfing [48].

[1] P. A. Sweet, in *IAU Symp. in Electromagnetic Phenomena in Cosmical Physics*, ed. B. Lehnert (New York: Cambridge Univ. Press) (1958), p. 123.

[2] E. N. Parker, *J. Geophys. Res.* **62**, 509 (1957).

- [3] H. E. Petschek, in *Proc. AAS-NASA Symp. Phys. Solar Flares* (1964), vol. 50 of *NASA-SP*, pp. 425–439.
- [4] S. Tsuneta, *Astrophys. J.* **456**, 840 (1996).
- [5] D. W. Longcope, S. E. Guidoni, and M. G. Linton, *Astrophys. J.* **690**, L18 (2009).
- [6] W. C. Feldman, S. J. Schwartz, S. J. Bame, D. N. Baker, J. T. Gosling, J. E. W. Hones, D. J. McComas, J. A. Slavin, E. J. Smith, and R. D. Zwickl, *Geophys. Res. Lett.* **11**, 599 (1984).
- [7] W. C. Feldman, R. L. Tokar, J. Birn, J. E. W. Hones, S. J. Bame, and C. T. Russell, *J. Geophys. Res.* **92**, 83 (1987).
- [8] E. J. Smith, J. A. Slavin, B. T. Tsurutani, W. C. Feldman, and S. J. Bame, *Geophys. Res. Lett.* **11**, 1054 (1984).
- [9] M. Øieroset, T. D. Phan, R. P. Lin, and B. U. Ö. Sonnerup, *J. Geophys. Res.* **105**, 25247 (2000).
- [10] M. Hoshino, T. Mukai, I. Shinohara, Y. Saito, and S. Kokubun, *J. Geophys. Res.* **105**, 337 (2000).
- [11] D. W. Walthour, J. T. Gosling, B. U. Ö. Sonnerup, and C. T. Russell, *J. Geophys. Res.* **99**, 23705 (1994).
- [12] D. W. Swift, *J. Geophys. Res.* **88**, 5685 (1983).
- [13] D. Winske, E. K. Stover, and S. P. Gary, *Geophys. Res. Lett.* **12**, 295 (1985).
- [14] N. Omid and D. Winske, *J. Geophys. Res.* **97**, 14801 (1992).
- [15] Y. Lin and L. C. Lee, *Space Science Reviews* **65**, 1 (1993).
- [16] L. Yin, D. Winske, W. Daughton, and F. V. Coroniti, *J. Geophys. Res.* **110** (2005).
- [17] L. Yin, D. Winske, and W. Daughton, *Phys. Plasmas* **14**, 062105 (2007).
- [18] J. F. Drake, M. Swisdak, T. D. Phan, P. A. Cassak, M. A. Shay, S. T. Lepri, R. P. Lin, E. Quataert, and T. H. Zurbuchen, *J. Geophys. Res.* **114**, 05111 (2009).
- [19] S. Bale, J. Kasper, G. G. Howes, E. Quataert, C. Salem, and D. Sundkvist, *Phys. Rev. Lett.* **103**, 211101 (2009).
- [20] R. F. Lottermoser, M. Scholer, and A. P. Matthews, *J. Geophys. Res.* **103**, 4547 (1998).
- [21] M. S. Nakamura, M. Fujimoto, and K. Maezawa, *J. Geophys. Res.* **103**, 4531 (1998).
- [22] Y. Lin and D. W. Swift, *J. Geophys. Res.* **101**, 19859 (1996).
- [23] M. Scholer and R. F. Lottermoser, *Geophys. Res. Lett.* **25**, 3281 (1998).
- [24] M. Cremer and M. Scholer, *Geophys. Res. Lett.* **26**, 2709 (1999).
- [25] M. Cremer and M. Scholer, *J. Geophys. Res.* **105**, 27621 (2000).
- [26] A. Zeiler, D. Biskamp, J. F. Drake, B. N. Rogers, M. A. Shay, and M. Scholer, *J. Geophys. Res.* **107**, 1230 (2002).
- [27] F. V. Coroniti, *Nucl. Fusion* **11**, 261 (1971).
- [28] Yi-Hsin Liu, J. F. Drake, and M. Swisdack, in preparation (2011).
- [29] B. U. Ö. Sonnerup, G. Paschmann, I. Papamastorakis, N. Sckopke, G. Haerendel, S. J. Bame, J. R. Asbridge, J. T. Gosling, and C. T. Russell, *J. Geophys. Res.* **86**, 10049 (1981).
- [30] J. T. Gosling, R. M. Skoug, D. J. McComas, and C. W. Smith, *J. Geophys. Res.* **110** (2005).
- [31] D. Krauss-Varban and N. Omid, *Geophys. Res. Lett.* **22**, 3271 (1995).
- [32] M. Hoshino, T. Mukai, and T. Yamamoto, *J. Geophys. Res.* **103**, 4509 (1998).
- [33] E. Mjølhus, *J. Plasma Phys.* **16**, 321 (1976).
- [34] S. R. Spangler and B. B. Plapp, *Phys. Fluids B* **4**, 3356 (1992).
- [35] A. Barnes and J. V. Hollweg, *J. Geophys. Res.* **79**, 2302 (1974).
- [36] D. Winske and N. Omid, *J. Geophys. Res.* **97**, 14779 (1992).
- [37] L. Yin, D. Winske, W. Daughton, and K. J. Bowers, *Phys. Plasmas* **14**, 062104 (2007).
- [38] R. C. Davidson and H. J. Volk, *Physics of Fluids* **11**, 2259 (1968).
- [39] D. Krauss-Varban, N. Omid, and K. B. Quest, *J. Geophys. Res.* **99**, 5987 (1994).
- [40] R. A. Treumann, *Astron. Astrophys. Rev.* **17**, 409 (2009).
- [41] E. A. Lucek, T. S. Horbury, M. W. Dunlop, P. J. Cargill, S. I. Schwartz, A. Balogh, P. Brown, C. Carr, K. H. Fornacon, and E. Georgescu, *Ann. Geophysicae* **20**, 1699 (2002).
- [42] M. Omid and D. Winske, *J. Geophys. Res.* **95**, 2281 (1990).
- [43] M. Scholer, *J. Geophys. Res.* **98**, 47 (1993).
- [44] A. R. Bell, *Mon. Not. R. astr. Soc.* **182**, 147 (1978).
- [45] M. A. Lee, *J. Geophys. Res.* **87**, 5063 (1982).
- [46] L. A. Fisk, G. Gloeckler, and T. H. Zurbuchen, *Astrophys. J.* **644**, 631 (2006).
- [47] R. B. Decker, *Space Science Reviews* **48**, 195 (1988).
- [48] R. Z. Sagdeev, *Reviews of Plasma Physics* **4**, 23 (1966).

Figures

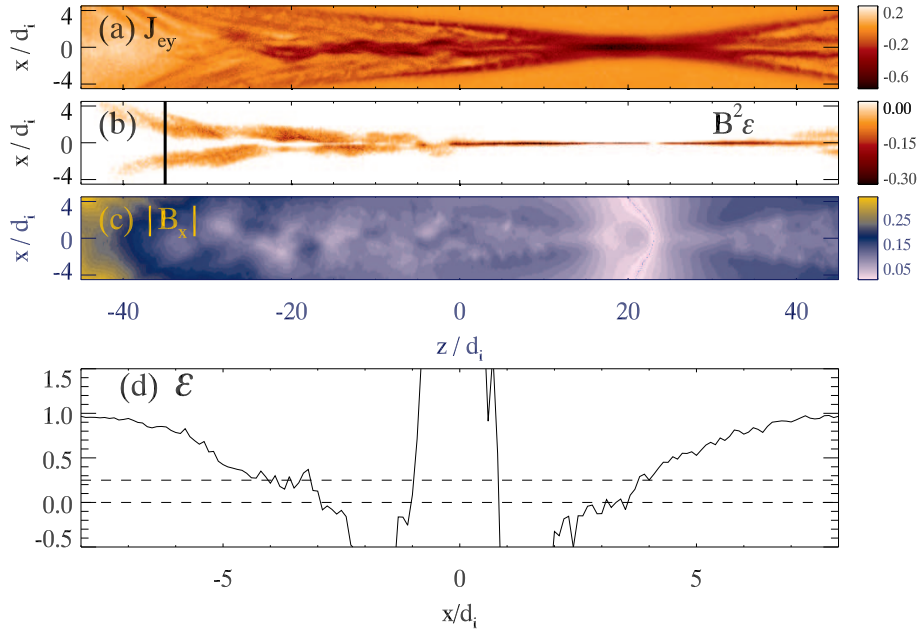


FIG. 1: The exhaust from steady reconnection in a PIC simulation. Panel (a): The out-of-plane electron current J_{ey} ; Panel (b): $B^2 \epsilon$, where positive values have been set to 0. The colored region is firehose unstable; Panel (c): The magnitude of B_x showing the turbulence associated with the firehose instability; Panel (d): A cut of ϵ at $x/d_i = -35$ (the vertical line in (b)). The horizontal lines demark $\epsilon = 0.25$ and $\epsilon = 0$.

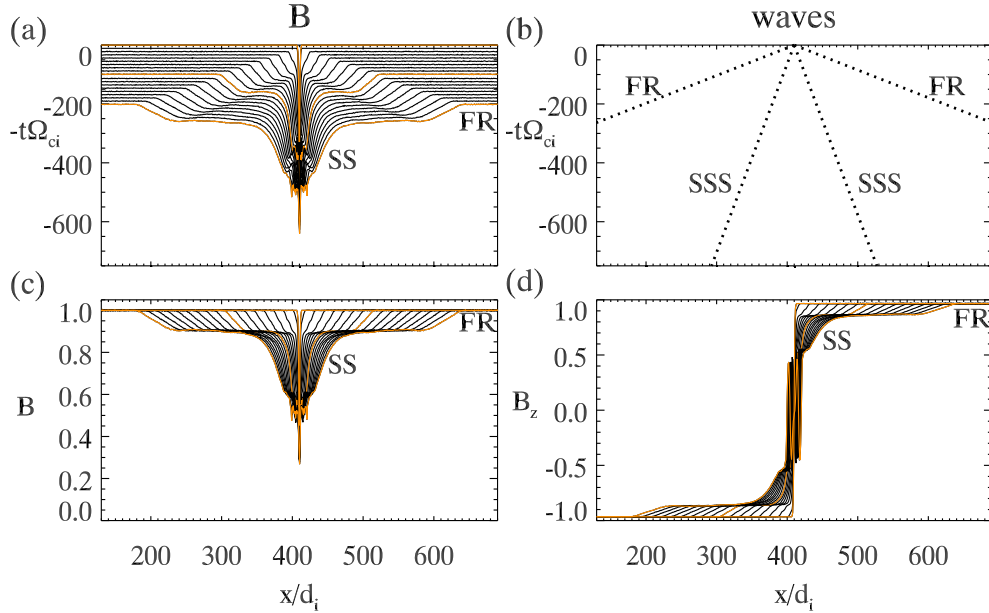


FIG. 2: The evolution of a system with $\theta_{BN} = 75^\circ$ (Run f). Panel (a): The evolution of B from time 0 – $200/\Omega_{ci}$. A pair of fast rarefactions (FR) propagate out from the symmetry line, followed by a pair of slow shocks (SS). Each curve has been shifted so that it intersects the vertical axis at the given time. The time between the yellow curves is $100/\Omega_{ci}$; Panel (b): The predicted FR and switch-off slow shock (SSS) from ideal MHD theory; Panel (c): The same as (a) but with the vertical axis measuring B ; Panel (d): The evolution of B_z from time 0 – $200/\Omega_{ci}$.

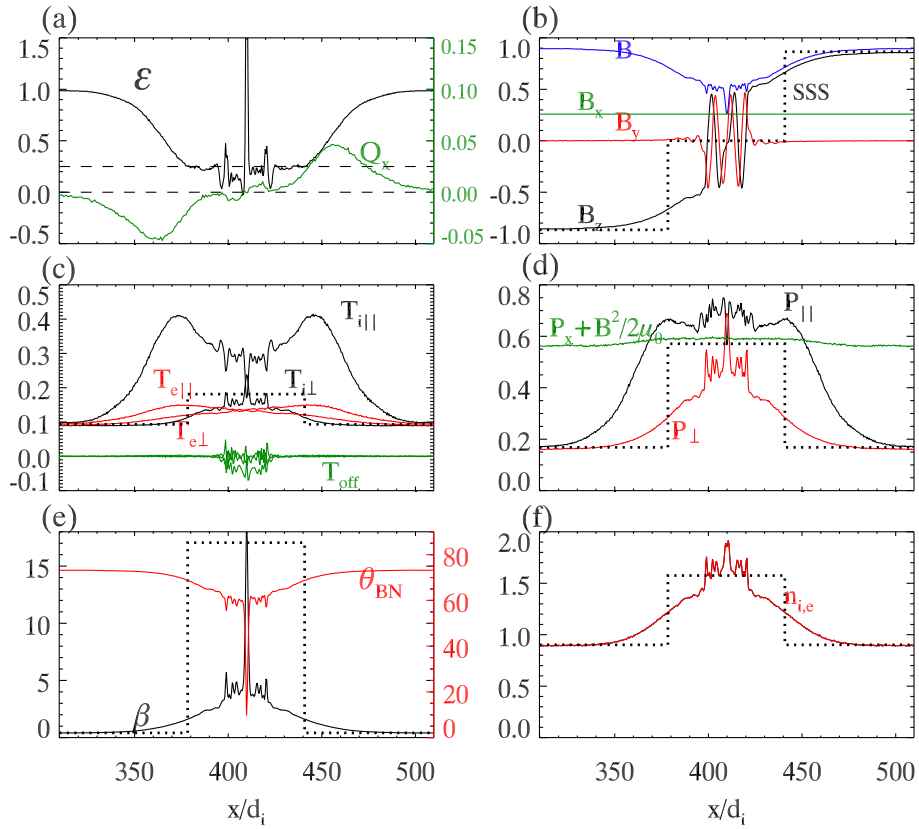


FIG. 3: Parameters from the run with $\theta_{BN} = 75^\circ$ (Run **f**) at time $200/\Omega_{ci}$. Panel (a): Temperature anisotropy ε and x -direction heat flux Q_x ; Panel (b): Magnetic field components; Panel (c): Parallel and perpendicular temperatures (the off-diagonal components $T_{ixy}, T_{ixz}, T_{iyz}$ are plotted together in green, denoted as T_{off} , and are small); Panel (d): Total plasma pressure components and $P_x + B^2/2\mu_0$. Panel (e): The plasma β and local $\theta_{BN} = \cos^{-1}(B_x/B)$; Panel (f): Plasma density. The dotted curves in each panel are the predicted magnitude and position of the switch-off slow shocks (SSS) from isotropic MHD for B_z in (b), T in (c), P in (d), β in (e), and n in (f).

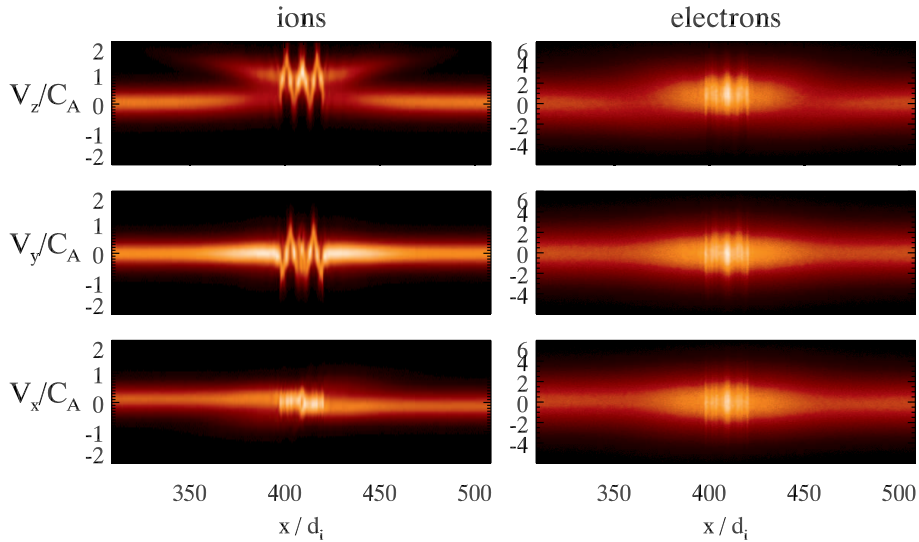


FIG. 4: The phase space of the run with $\theta_{BN} = 75^\circ$ (Run **f**) at time $200/\Omega_{ci}$. From top to bottom the left column shows the ion distribution in: $V_z - x$ space, where the backstreaming ions from the discontinuities are clearly seen; $V_y - x$ space; $V_x - x$ space. The right column is the electron distribution in $V_z - x$ space, $V_y - x$ space and $V_x - x$ space.

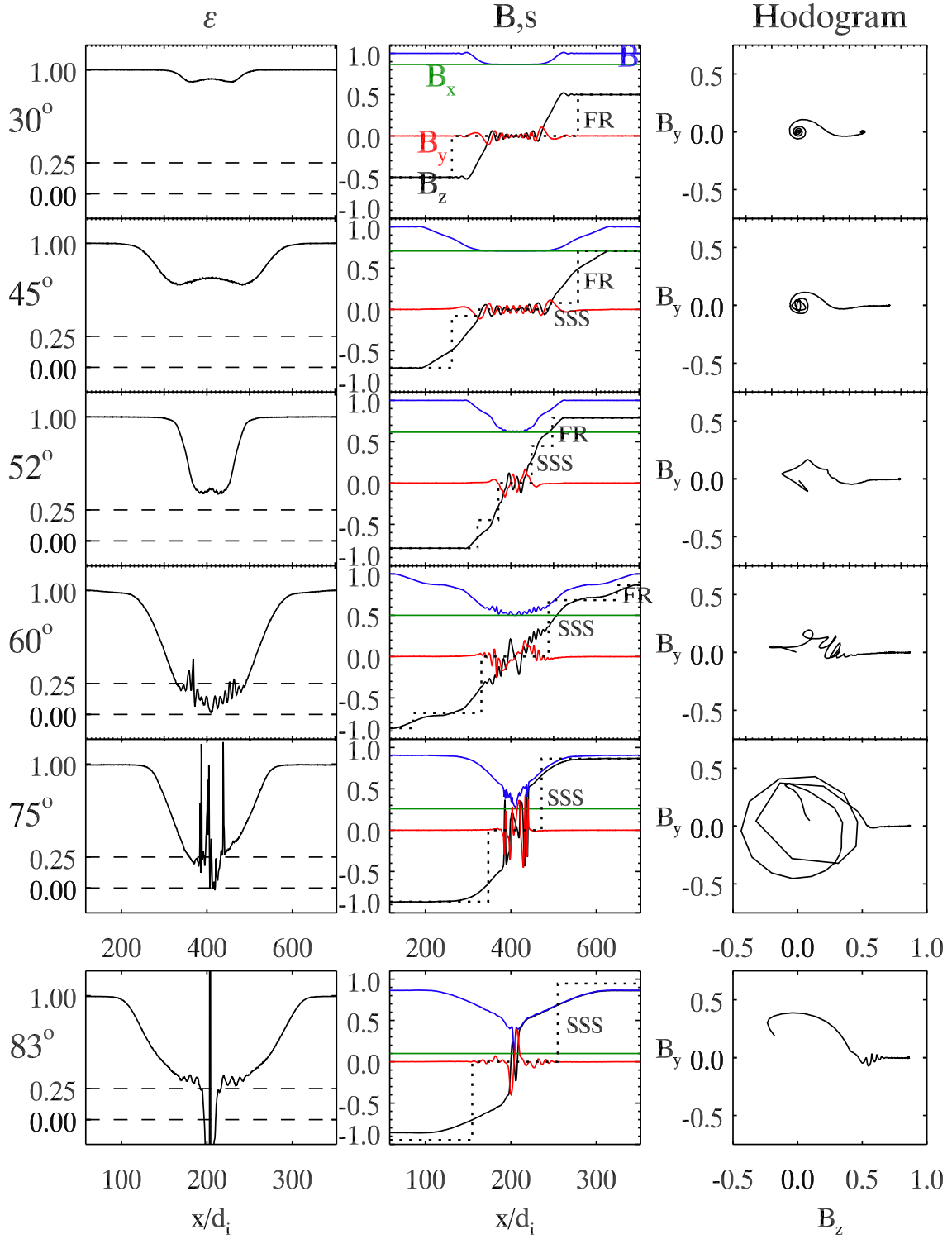


FIG. 5: From top to bottom are runs with $\theta_{BN} = 30^\circ$ (Run a) at $100/\Omega_{ci}$, 45° (Run b) at $200/\Omega_{ci}$, 52° (Run c) at $100/\Omega_{ci}$, 60° (Run d) at $250/\Omega_{ci}$, 75° (Run f) at $400/\Omega_{ci}$, and 83° (Run k) at $700/\Omega_{ci}$. The first column shows the temperature anisotropy, and the second column the magnetic field components as a function of x . The third column displays hodograms taken from the right half of the simulation domains. The dotted curves in the second column are the predicted magnitudes and positions of switch-off slow shocks (SSS) and fast rarefactions (FR) from isotropic MHD theory.

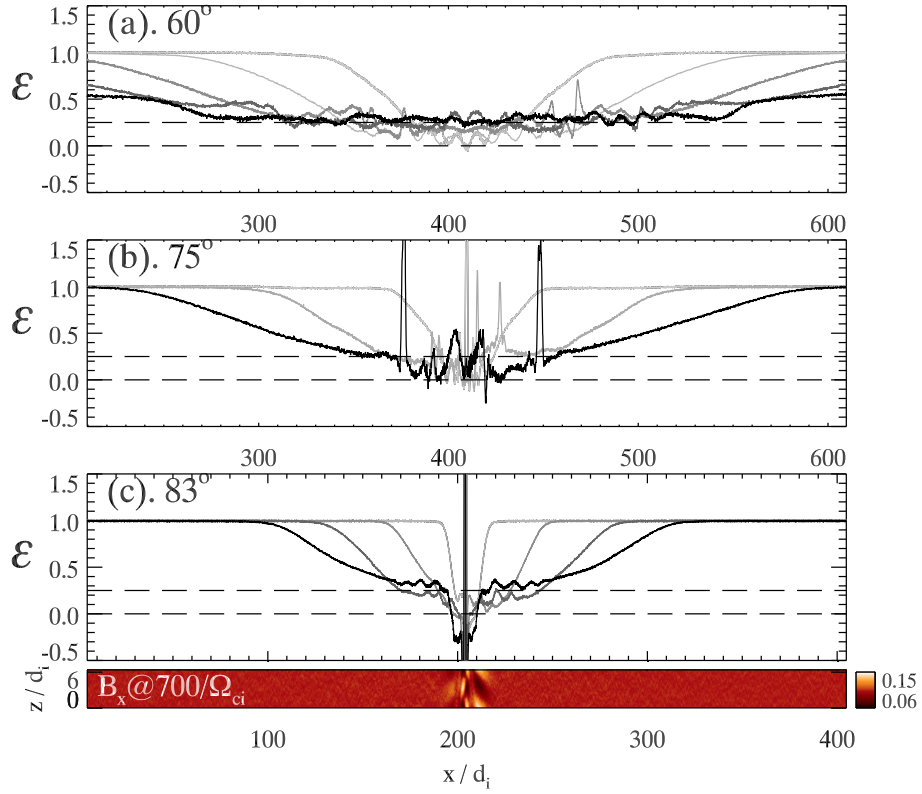


FIG. 6: Evolution of ε for the case with $\theta_{BN} = 60^\circ$ (Run d) for equally spaced times between $100 - 500/\Omega_{ci}$ from lighter grey to darker grey in (a), the $\theta_{BN} = 75^\circ$ case (Run f) for time $100 - 500/\Omega_{ci}$ in (b), and the $\theta_{BN} = 83^\circ$ case (Run k) for time $100 - 700/\Omega_{ci}$ in (c). The bottom is a plot of B_x for the $\theta_{BN} = 83^\circ$ case at time $700/\Omega_{ci}$ showing the 2-D turbulence that develops.

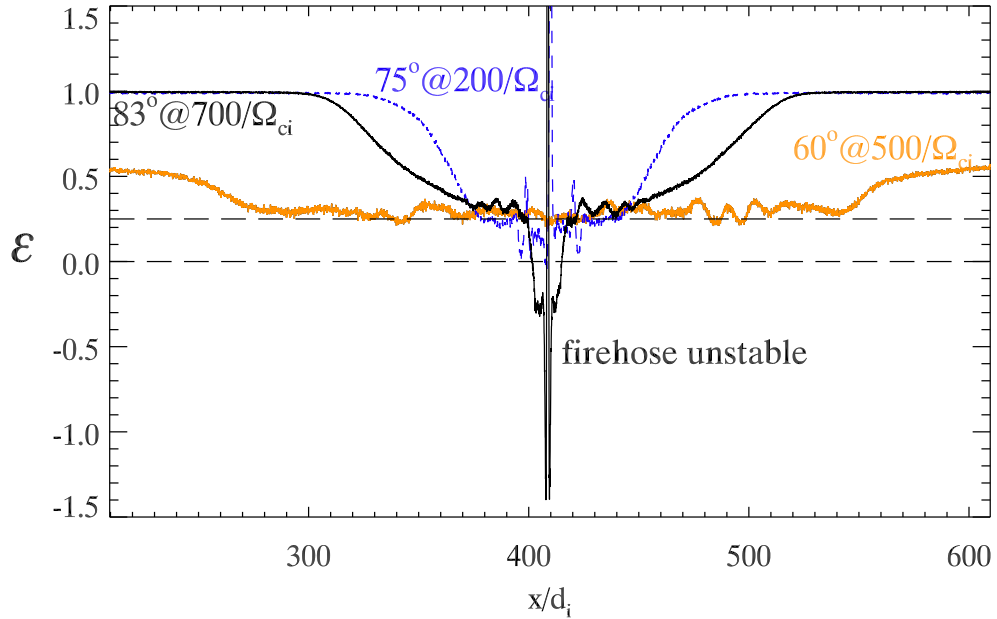


FIG. 7: The ε distributions of runs $\theta_{BN} = 60^\circ$ (Run d) at $500/\Omega_{ci}$, 75° (Run f) at $200/\Omega_{ci}$, 83° (Run k) at $700/\Omega_{ci}$. (The 83° case is shifted to the right by $204.8d_i$)

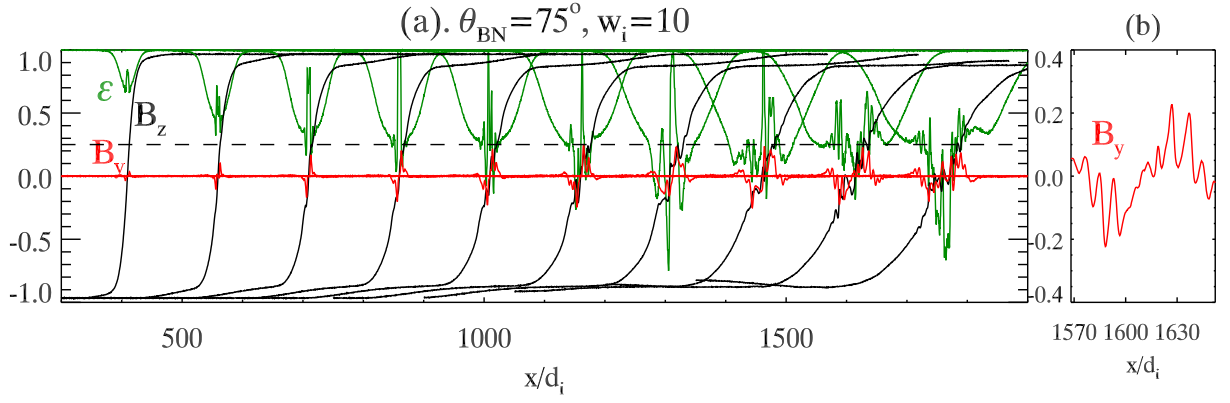


FIG. 8: Panel (a): The evolution of ε , B_z and B_y for equally spaced times between $50 - 500/\Omega_{ci}$ (from left to right) in the $\theta_{BN} = 75^\circ$, $w_i = 10d_i$ case (Run **g**). The downstream larger-scale rotational wave breaks into waves of wavelength $\sim 6d_i$. Panel (b): A blowup of the downstream B_y at time $450/\Omega_{ci}$.

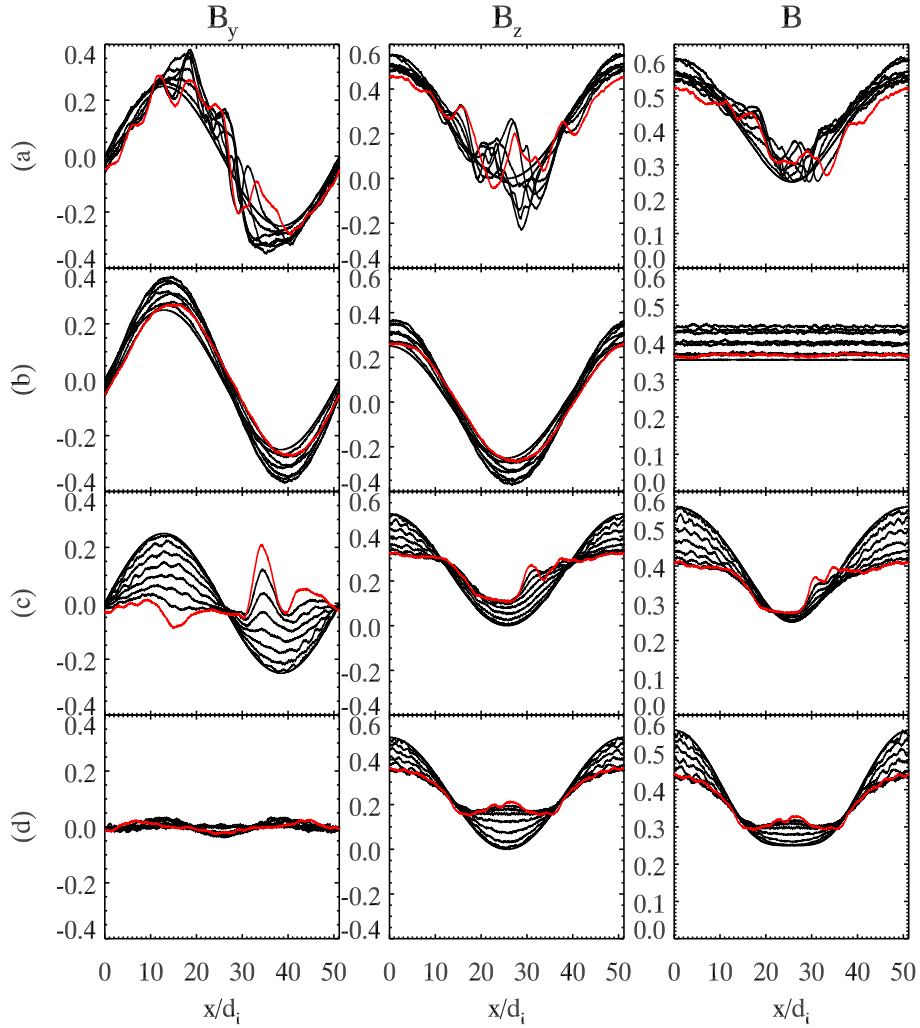


FIG. 9: The evolution of B_y , B_z and B for equally spaced times between $0 - 100/\Omega_{ci}$. The red curve indicates the time $100/\Omega_{ci}$. Panel (a): Run **1** with both initial streaming ions and modulated rotational parent wave. Panel (b): The same as panel (a) without the initial spatial modulation (Run **3**). Panel (c): The same as panel (a) without initial beams (Run **5**). Panel (d): The same as panel (c) without initial polarization (Run **6**).

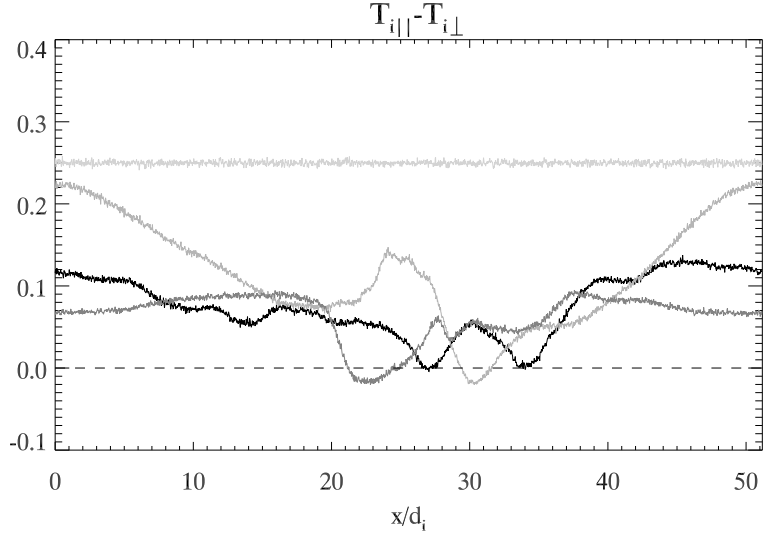


FIG. 10: The evolution of $T_{i||} - T_{i\perp}$ for equally spaced times between $0 - 100/\Omega_{ci}$ (from lighter grey to darker grey) of Run 1 (Fig. 9(a)). The temperature anisotropy of the ions is reduced, which indicates particle scattering is taking place.

Tables

TABLE I:

Run	θ_{BN}	w_i	B_g^a	Domain Size ($l_z \times l_x$)	Gridpoints	\rightarrow^b 2-D turbulence
a	30°	1	0	1.6×1638.4	64×65536	x
b	45°	1	0	1.6×1638.4	64×65536	x
c	52°	1	0	1.6×1638.4	64×65536	x
d	60°	1	0	1.6×1638.4	64×65536	x
e	60°	1	0	6.4×819.2	256×32768	x
f	75°	1	0	1.6×1638.4	64×65536	x
g	75°	10	0	1.6×1638.4	64×65536	x
h	75°	1	0.2	1.6×1638.4	64×65536	x
i	75°	1	0	6.4×1638.4	256×65536	✓
j	83°	1	0	1.6×819.2	64×32768	x
k	83°	1	0	6.4×819.2	256×32768	✓

^a B_g is an initial uniform guide field in the y-direction

^b“ \rightarrow ” means “resulting in”.

TABLE II:

Run	B_{cir}	Polarization(P)	$B_{z,oblique}$	$T_{i }$	Beams (u)	$\rightarrow^a T_{i ,eff}$	$\rightarrow \varepsilon$	\rightarrow 1-D d_i -scale waves ($t < 100/\Omega_{ci}$)
1	0.25	+1	0.25	0.15	0.5	0.4	-0.2 ~ -7	✓
2	0.25	+1	0.25	0.4	0	0.4	-0.2 ~ -7	✓
3	0.25	+1	0	0.15	0.5	0.4	-2	x
4	0.25	+1	0	0.4	0	0.4	-2	x
5	0.25	+1	0.25	0.15	0	0.15	1	✓
6	0.25	0	0.25	0.15	0	0.15	1	x

^a“ \rightarrow ” means “resulting in”.